

Firing dynamics in a second-order memcapacitor-based FitzHugh-Nagumo neuron with multiscale memory

Zhijun Li(李志军) and Pengyang Li(李鹏洋)

Citation: Chin. Phys. B, 2026, 35 (**6**): 060505. DOI: 10.1088/1674-1056/ae4c6b
http://cpb.iphy.ac.cn; http://iopscience.iop.org/cpb

What follows is a list of articles you may be interested in

Meminductor synaptic coupling in a heterogeneous HR-FHN neuron network: Model, dynamics, and DSP implementation

Yang Yin(尹扬) and Zhijun Li(李志军)
Chin. Phys. B, 2026, 35 (**6**): 060503. DOI: 10.1088/1674-1056/ae56e2

Fixed points as regulatory hubs in discrete memristive neural networks: An analysis of the FitzHugh-Nagumo model

Shaobo He(贺少波), Jiawei Xiao(肖佳伟), Qilai Chen(陈祺来), and Huihai Wang(王会海)
Chin. Phys. B, 2026, 35 (**6**): 060502. DOI: 10.1088/1674-1056/ae3131

Double coherence resonance of the FitzHugh–Nagumo neuron driven by harmonic velocity noise

Song Yan-Li (宋艳丽)
Chin. Phys. B, 2014, 23 (**8**): 080504. DOI: 10.1088/1674-1056/23/8/080504

SPECIAL TOPIC — Biophysical circuits: Modeling & applications in neuroscience

Firing dynamics in a second-order memcapacitor-based FitzHugh–Nagumo neuron with multiscale memory

Zhijun Li(李志军)[†,‡] and Pengyang Li(李鹏洋)[†,§]

School of Automation and Electronic Information, Xiangtan University, Xiangtan 41110, *China*

(Received 19 December 2025; revised manuscript received 26 February 2026; accepted manuscript online 3 March 2026)

This paper presents a second-order memcapacitor (C_M)-based FitzHugh–Nagumo (FHN) neuron model designed to emulate multiscale memory mechanisms observed in biological neurons. The memcapacitor incorporates two internal state variables — a fast variable that enables rapid response and a slow variable that enables gradual adaptation — replacing the linear membrane capacitor in the classical FHN circuit to form a four-dimensional neuronal system. The electrical activities of the neuron are systematically investigated using bifurcation diagrams, Lyapunov exponents, and a twoparameter dynamical map. Numerical simulations reveal that variations in excitation frequency and amplitude can induce transitions among chaotic firing, multiperiodic firing, and single-periodic spiking. Furthermore, the model demonstrates pronounced multistability governed by the memcapacitor's initial states, where distinct periodic and chaotic attractors coexist within separate basins of attraction — a direct manifestation of the multiscale memory interaction. By tailoring external stimuli and internal parameters, the neuron successfully reproduces eight quintessential neuromorphic behaviors, including phasic and tonic spiking, mixed-mode oscillations, subthreshold oscillations, inhibition-induced spiking, rebound spikes, bistability, and Class 2 excitability. Finally, an analog FHN circuit integrated with a secondorder memcapacitor emulator is implemented using off-the-shelf electronic components. Circuit simulations demonstrate excellent agreement with numerical analyses, thereby validating both the model's correctness and its physical realizability for neuromorphic engineering applications.

Keywords: second-order memcapacitor, FitzHugh–Nagumo neuron, firing dynamics, neuromorphic computing

PACS: 05.45.Tp, 87.19.ld, 05.90.+m, 05.45.–a

DOI: 10.1088/1674-1056/ae4c6b **CSTR:** 32038.14.CPB.ae4c6b

1. Introduction

Artificial neural systems and neuromorphic circuits aim to replicate the rich firing activities of biological neurons while maintaining low power consumption and compact hardware implementation. Among various mathematical neuron models, the FitzHugh–Nagumo (FHN) model[1–3] has emerged as a widely adopted simplification of the Hodgkin–Huxley formalism.[4,5] With only two state variables, it captures essential excitable properties and canonical firing patterns, making it well suited for dynamical analysis and analog circuit implementation. However, the classical FHN circuit, constructed from one linear resistor, one inductor, one capacitor, and one nonlinear resistor, inherently lacks memory mechanisms. This limitation significantly restricts its ability to reproduce the complex history-dependent behaviors observed in biological neural systems.

To address this fundamental limitation, researchers have increasingly turned to memory circuit elements. The memristor,[6–9] first postulated by Chua in 1971 and physically realized in 2008, has become a cornerstone in neuromorphic engineering. These devices naturally combine nonlinearity with nonvolatile memory, enabling compact emulation of synaptic plasticity, autapse coupling, and electromagnetic effects. Nevertheless, practical challenges remain, including relatively high energy consumption during frequent switching operations and sensitivity to low-amplitude noise, which can degrade the stability of the firing patterns in hardware implementations.

In parallel, the memcapacitor[10–12] concept has emerged as a promising alternative. These devices exhibit a memory-dependent charge–voltage relationship, allowing history-modulated charge storage. Recent studies have demonstrated their potential for building energy-efficient neuron circuits, revealing phenomena such as hidden electrical activity,[13,14] complex bursting patterns,[15,16] and extreme multistability.[17–19] However, most existing work has primarily focused on first-order memcapacitors. For instance, Wang *et al.*[20] developed a memcapacitor-based cellular neural network (MC-CNN) model with infinitely many equilibrium points, demonstrating complex attractors and hardware real-

[†]These authors contributed equally to this work.

[‡]Corresponding author. E-mail: lizhijun@xtu.edu.cn

[§]Corresponding author. E-mail: 1936260040@qq.com

© 2026 Chinese Physical Society and IOP Publishing Ltd. All rights, including for text and data mining, AI training, and similar technologies, are reserved.

izability. Ge *et al.*[21] proposed a memristor–memcapacitor-coupled FHN neuron, showing that dual regulation by the two memory elements enables rich firing transitions and noise-induced stochastic resonance/coherent resonance phenomena.

A critical examination of current research reveals significant limitations in existing memory element implementations. First, most memcapacitor-based neuronal models employ first-order devices with a single memory timescale,[22,23] which fundamentally contradicts the biological reality of neural memory. Second, current implementations lack the capacity to emulate the intricate temporal dynamics where short-term adaptation (milliseconds to seconds) and long-term plasticity (minutes to lifetimes) coexist and interact within biological neurons. Third, integrating multiple memory mechanisms typically requires complex circuit arrangements involving multiple discrete components, increasing hardware complexity and power consumption. Biological systems provide compelling evidence for multiscale memory mechanisms. Neural circuits exhibit diverse temporal dynamics ranging from rapid synaptic depression (tens of milliseconds) to long-term potentiation (hours to days). These mechanisms operate simultaneously, enabling neurons to process information across different timescales[24–26] — a capability crucial for learning, adaptation, and complex cognitive functions. Short-term mechanisms facilitate rapid signal processing and dynamic modulation, while long-term mechanisms underlie information consolidation and structural reorganization. Current neuromorphic implementations fail to capture this essential multiscale nature, representing a significant gap between biological inspiration and engineering realization.

This research gap presents both a challenge and an opportunity. While first-order memory elements have advanced neuromorphic computing,[27,28] their limited temporal dynamics restrict their biological fidelity and functional versatility. There exists a pressing need for memory devices that can inherently support multiple timescales within a single compact structure. Such devices would enable more biologically realistic neural models while maintaining the hardware efficiency essential for practical applications.

To bridge this gap, the present study first establishes a novel second-order memcapacitor model with dual-timescale memory, then constructs a four-dimensional FHN neuron by replacing the conventional capacitor with this element, and finally performs comprehensive dynamical analysis alongside experimental circuit validation. Within this framework, the work introduces three fundamental innovations:

First, we propose a novel second-order memcapacitor architecture that extends conventional memory element design by incorporating two distinct internal state variables: a fast variable representing transient state changes responsive to input signals, and a slow variable capturing cumulative long-term effects with gradual saturation characteristics. This dual-timescale design enables a single device to emulate both short-term adaptation and long-term plasticity — mechanisms that typically require separate implementations in conventional neuromorphic circuits.

Second, we develop a comprehensive second-order memcapacitor-based FHN neuron model that replaces the conventional linear capacitor with our advanced memory element. The resulting four-dimensional system maintains the computational efficiency of the classic FHN framework while incorporating biologically inspired multiscale memory. Theoretical analysis confirms this structure creates rich dynamical spaces where memory effects operate across different temporal domains, closely mimicking biological neural systems.

Third, our implementation demonstrates unprecedented functional capabilities including: (i) accurate emulation of biological memory mechanisms without increasing circuit complexity; (ii) enhanced control over neuronal dynamics through multiple accessible parameters; and (iii) full compatibility with standard analog circuit design methodologies for practical hardware realization.

This paper is organized as follows: Section 2 introduces the second-order memcapacitor model and characterizes its hysteretic properties. Section 3 presents the memcapacitor-based FHN neuron and analyzes its equilibrium states. Section 4 investigates parameter-dependent and initial-value-dependent firing dynamics, including the reproduction of classical neuromorphic behaviors. Section 5 presents other neuromorphic behaviors. Section 6 details the circuit implementation and provides experimental validation. Finally, Section 7 concludes with a summary of findings and perspectives for future research.

2. Second-order memcapacitor model and its characteristics

2.1. Second-order memcapacitor model

A second-order memcapacitor is characterized by its ability to embed dual-timescale memory effects via two internal state variables. The relationship between the voltage v across the device and the stored charge q is given by

$$v = C_{\mathrm{M}}^{-1}(x_1, x_2)q. \tag{1}$$

Here, C_{M} represents the memory-dependent capacitance, and x_1 and x_2 represent the fast and slow internal state variables, respectively. Their dynamics are described by the following coupled differential equations:

$$\begin{cases} \dfrac{\mathrm{d}x_1}{\mathrm{d}t} = f_1(x_1, q) = a_1 q - b_1 x_1, \\ \dfrac{\mathrm{d}x_2}{\mathrm{d}t} = f_2(x_2, q) = a_2 q^2 - b_2 \tanh(x_2). \end{cases} \tag{2}$$

The resulting inverse memcapacitance is governed by

$$C_{\mathrm{M}}^{-1} = \alpha + \beta x_1 + \lambda \tanh(x_2), \tag{3}$$

where α, β, λ, a_1, a_2, b_1, and b_2 are constant parameters. The first state variable x_1 captures transient, rapidly decaying memory effects, whereas the slow variable x_2 accumulates long-term, gradually saturating memory contributions. In Eq. (2), a_1 and b_1 mainly shape the fast memory state x_1: a_1 controls the input-driven response and b_1 sets the decay rate, so x_1 can be interpreted as a short-term adaptation process. Likewise, a_2 and b_2 govern the slow state x_2, where a_2 determines the accumulation strength and b_2 governs the slow relaxation process with saturation, corresponding to long-term plasticity. In Eq. (3), α provides the baseline inverse memcapacitance, while β and λ weight the contributions of the fast (x_1) and slow (x_2) memory states to the effective capacitance. By incorporating both short-term and long-term memory, the proposed second-order memcapacitor enriches the system dynamics, enabling bifurcations, multistability, and chaos that are important for modeling history-dependent neural activity.

2.2. Hysteresis loop analysis

To validate the memcapacitive nature of the proposed model, we examine its response under a sinusoidal current excitation $i(t) = I_{\mathrm{S}} \cos(\omega t)$ in a systematic and reproducible numerical framework. The parameters are fixed as $a_1 = 0.8$, $b_1 = 0.5$, $a_2 = 0.5$, $b_2 = 0.5$, $\alpha = 1.0$, $\beta = 0.5$, and $\lambda = -0.3$, which are maintained unless otherwise noted during the analysis.

Figure 1(a) shows the hysteresis loop area in the q–v plane for the fixed frequency $\omega = 1.0$ and different excitation amplitudes I_{S}. It is observed that as I_{S} increases from 1.0 to 3.0, the loop area expands significantly, indicating a stronger memory effect under larger stimuli. Similarly, Fig. 1(b) displays the loops for a fixed amplitude $I_{\mathrm{S}} = 2.0$ and varying frequencies ω. As observed, with increasing ω, the loop shrinks, reflecting the frequency-dependent fading of the memory signature. These results confirm that the proposed second-order memcapacitor not only retains the fundamental pinched-hysteresis property, but also offers tunable memory strength through both amplitude and frequency modulation — a capability that is particularly valuable for reconfigurable neuromorphic circuits.

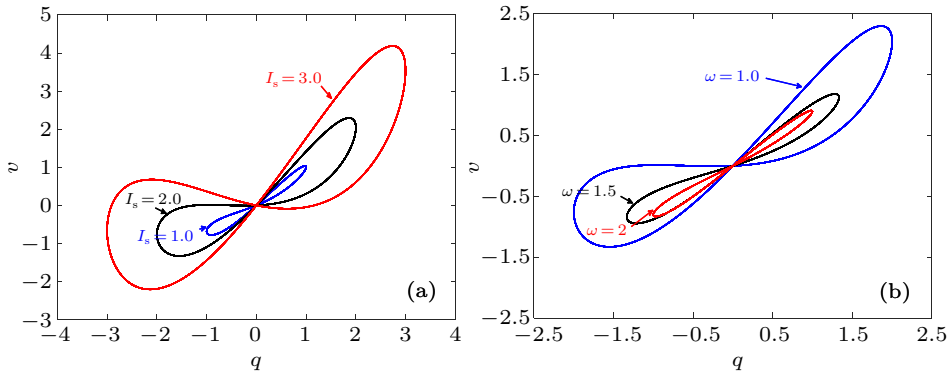


Fig. 1. Pinched hysteresis loops of the second-order memcapacitor: (a) amplitude-dependent hysteresis loops under fixed frequency $\omega = 1.0$, (b) frequency-dependent hysteresis loops under fixed amplitude $I_{\mathrm{S}} = 2.0$.

3. FHN neuron based on second-order memcapacitor

3.1. Description of FHN neuron model

Figure 2 illustrates the FHN neuron circuit in which the classical linear capacitor is replaced by the proposed second-order memcapacitor. Biophysically, this replacement implies that the constant membrane-capacitance assumption in the classical FHN circuit is generalized to a history-dependent effective capacitance, allowing the "membrane" to store and release charge in a manner that depends on its previous activity. The introduced fast and slow internal memory states naturally support adaptive responses and long-term modulation of excitability, thereby enabling the reproduction of history-dependent firing behaviors beyond those achievable with a linear capacitor. The circuit comprises an inductor L, a memcapacitor C_{M}, a resistor R, and a nonlinear resistor R_{N}. Through circuit analysis, the system dynamics of the second-order memcapacitor-based FHN neuron can be derived as

$$\begin{cases} \dfrac{\mathrm{d}i_{\mathrm{L}}}{\mathrm{d}t} = \dfrac{R_0}{L}\left(\dfrac{v}{R_0} - \dfrac{R}{R_0} i_{\mathrm{L}}\right), \\ \dfrac{\mathrm{d}q}{\mathrm{d}t} = i_{\mathrm{S}} - i_{\mathrm{L}} - i_{\mathrm{RN}}, \\ \dfrac{\mathrm{d}x_1}{\mathrm{d}t} = a_1 q - b_1 x_1, \\ \dfrac{\mathrm{d}x_2}{\mathrm{d}t} = a_2 q^2 - b_2 \tanh(x_2), \end{cases} \tag{4}$$

where v represents the voltage across the second-order memcapacitor, i_{L} is the inductor current, $i_{\mathrm{RN}} = -(v - \frac{1}{3}v^3)/\rho$ represents the current through the nonlinear resistor (with $\rho = 1$), and $i_{\mathrm{S}} = F\cos(\omega t)$ is an external sinusoidal stimulus.

To clarify the physical meaning of the state variables in the normalized model, we define $x = i_{\mathrm{L}}$ as the inductor cur-

rent and $y = q$ as the charge stored in the memcapacitor. The memcapacitor contains two internal state variables, x_1 and x_2, corresponding to fast and slow memory dynamics (denoted as z and e in Eq. (5)), respectively, which characterize the multi-scale memory effect of the device.

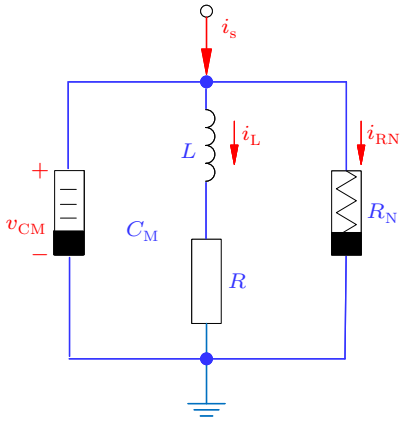


Fig. 2. The second-order memcapacitor-based FHN neuron circuit.

For normalization, the physical parameters are grouped as $a = 1/L$ and $c = R/L$. Here, a reflects the intrinsic response rate determined by the inductance L, while c represents the effective damping introduced by the linear resistor R. This normalization reduces parameter redundancy and highlights the essential dynamical structure of the system. With these substitutions, Eq. (4) is transformed into the dimensionless four-dimensional neuron model given in

$$\begin{cases} \dot{x} = av - cx, \\ \dot{y} = F\cos(\omega t) - x + v - \dfrac{1}{3}v^3, \\ \dot{z} = a_1 y - b_1 z, \\ \dot{e} = a_2 y^2 - b_2 \tanh(e), \end{cases} \tag{5}$$

with

$$v = C_{\mathrm{M}}^{-1}(z, e)y. \tag{6}$$

This model preserves the excitable structure of the classical FHN system while embedding dual-timescale memory through the internal variables z and e. The memcapacitive coupling introduces a history-dependent modulation of the membrane voltage, enabling adaptive firing behaviors that cannot be reproduced by conventional linear-capacitor counterparts. Compared with the classical FHN model, this formulation introduces two additional state variables, resulting in only a modest increase in computational cost per simulation and remaining readily tractable with standard ODE solvers. In practice, numerical reliability can be verified by confirming that the main firing patterns remain unchanged when a smaller integration step size is adopted. If the proposed neuron is extended to network-level simulations in future work, the computational burden will primarily increase with the number of neurons, while sparse connectivity may help maintain good scalability.

3.2. Equilibrium points analysis

The parameters are set as $a = 1.0$ and $c = 0.6$. To investigate the influence of the external excitation $i_{\mathrm{S}} = F\cos(\omega t)$, we consider the so-called AC equilibrium points of the non-autonomous system. These points are defined as the solutions of the steady-state conditions obtained by setting all time derivatives in system (5) to zero

$$\dot{x} = 0, \ \ \dot{y} = 0, \ \ \dot{z} = 0, \ \ \dot{e} = 0.$$

The AC equilibrium point can be expressed as $E_{\mathrm{AC}} = (x_{\mathrm{e}}, y_{\mathrm{e}}, z_{\mathrm{e}}, e_{\mathrm{e}})$, where

$$\begin{aligned} x_{\mathrm{e}} &= \frac{a}{c}v_{\mathrm{e}}, \ \ z_{\mathrm{e}} = \frac{a_1}{b_1}y_{\mathrm{e}}, \ \ \tanh(e_{\mathrm{e}}) = \frac{a_2}{b_2}y_{\mathrm{e}}^2, \\ v_{\mathrm{e}} &= \left(\alpha + \beta\frac{a_1}{b_1} + \lambda\frac{a_2}{b_2}y_{\mathrm{e}}^2\right)y_{\mathrm{e}}, \end{aligned} \tag{7}$$

and the coordinate y_{e} is determined by solving

$$G(i_{\mathrm{S}}, y_{\mathrm{e}}) = \left(1 - \frac{a}{c}\right)v_{\mathrm{e}} - \frac{1}{3}v_{\mathrm{e}}^3 + i_{\mathrm{S}} = 0. \tag{8}$$

The local stability of each AC equilibrium point is assessed through linearization. Specifically, the eigenvalues of the Jacobian matrix evaluated at E_{AC} are computed. An equilibrium point is classified as stable if all eigenvalues have negative real parts, whereas it is classified as an unstable saddle-focus if one or more eigenvalues possess positive real parts. The instability index is defined as the number of eigenvalues with positive real parts, providing a quantitative measure of the instability of the equilibrium point. Figure 3 illustrates the branch of E_{AC} in the i_{S}–y_{e} plane, where the colors denote different stability types: stable (yellow), index-1 saddle-focus (blue), and index-2 saddle-focus (orange). It can be observed that the number, location, and stability of the AC equilibrium points vary significantly with changes in the external excitation i_{S}.

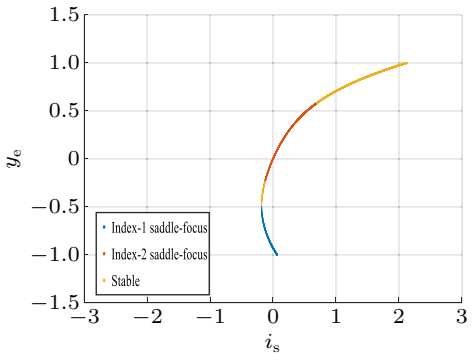


Fig. 3. AC equilibrium branches in the (i_{S}, y_{e}) plane, with colors indicating stability types: stable (yellow), index-1 saddle-focus (blue), and index-2 saddle-focus (orange).

4. Firing dynamics in the proposed FHN neuron

This section analyzes the effects of excitation frequency, amplitude, and initial conditions on the firing behavior of the second-order memcapacitor-based FHN neuron model. The bifurcation diagrams are calculated using the ODE45 algorithm in Matlab with a time step of 10^{-2}, and Lyapunov exponents are computed using the Jacobi matrix-based method with a time step of 10^{-3}.

4.1. Excitation frequency-dependent electrical activity

This section examines how the excitation frequency ω modulates the firing dynamics of the proposed second-order memcapacitor-based FHN neuron. The excitation amplitude is fixed at $F = 0.125$, with the initial conditions set to $(x, y, z, w) = (0.1, 0.1, -0.1, 0.3)$.

Figure 4(a) shows the bifurcation diagram of the membrane voltage as ω varies from 0 to 0.8. The corresponding Lyapunov exponents are displayed in Fig. 4(b). Collectively, these plots reveal a rich sequence of frequency-induced transitions among distinct firing regimes, with the maximum Lyapunov exponent (LE1) serving as a key indicator of chaos (LE1 > 0) or periodicity (LE2 ≤ 0). At very low frequencies ($\omega \in [0, 0.2)$), the membrane voltage exhibits adiabatic tracking of the slowly varying AC equilibrium branches. The neuron's trajectory closely follows the stable segments of the equilibrium structure, with transitions between spiking and silent phases occurring near stability-change points. In this range, Lyapunov exponents remain near zero or slightly negative ($\lambda_1 \approx 0$), indicating marginal stability or weak chaotic fluctuations embedded within the quasi-static response. At $\omega = 0.03$ (Figs. 5(a) and 5(b)), clear quasi-static modulation is observed: the time-series of v aligns closely with the AC equilibrium branches while the phase portrait displays irregular yet bounded orbits shaped by the equilibrium manifold — a behavior consistent with near-zero Lyapunov exponents. At $\omega = 0.14$ (Figs. 5(c) and 5(d)), tracking becomes less precise and spiking grows increasingly irregular; LE1 remains slightly above zero, suggesting an onset of weakly chaotic dynamics while still loosely guided by equilibrium structures.

As the excitation frequency increases beyond $\omega = 0.2$, assumptions regarding quasi-static behavior gradually break down due to rapid variations in the external input that exceed the neuron's ability to follow instantaneous equilibrium branches; consequently, firing dynamics become dominated by intrinsic oscillator properties. When $\omega \in [0.3, 0.45]$, the bifurcation diagram displays multiple continuous branches (Fig. 4(a)), with all Lyapunov exponents negative (Fig. 4(b)), signifying periodic bursting behavior. As demonstrated in Figs. 6(a) and 6(b), the phase portrait and time series show regular bursting oscillations at $\omega = 0.4$. As ω approaches 0.46, the multiperiodic firing gradually evolves into chaos through a period-doubling route to chaos, characterized by the accumulation of bifurcations and increasing orbit complexity rather than an abrupt transition. As the frequency $\omega \in [0.46, 0.51)$, the neuron enters a chaotic window characterized by a positive maximum Lyapunov exponent (LE1 > 0) and irregular, densely scattered bifurcation points. For $\omega = 0.5$ (Figs. 6(c) and 6(d)), the phase portrait and time series display complex aperiodic oscillations, directly correlating with the positive LE1 that confirms deterministic chaos. When $\omega \in [0.52, 0.75]$, the bifurcation branches narrow and stabilize. Lyapunov exponents return to negative values (LE1 < 0), indicating the recovery of periodic dynamics. This transition from chaos to periodicity occurs progressively, as the chaotic attractor contracts and reorganizes into multiperiodic oscillations, which further simplify into a stable period-2 rhythm – a process corresponding to a reverse period-doubling. At $\omega = 0.55$ (Figs. 6(e) and 6(f)), multiperiodic firing is observed – the phase portrait shows distinct loops corresponding to different periods, and the time series exhibits periodic bursts with varying intervals. Finally, for $\omega > 0.75$, the bifurcation diagram exhibits densely scattered, disordered points, and λ_1 again becomes positive, indicating a re-entry into chaotic firing. Notably, the transition from period-2 firing to chaos occurs abruptly, accompanied by a sudden expansion of the attractor, which is indicative of a boundary-crisis-induced transition.

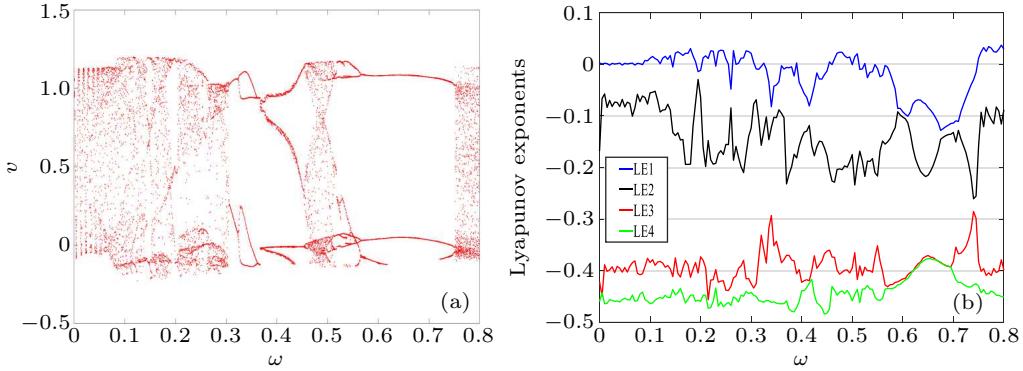


Fig. 4. Bifurcation diagram of the state variable v and the corresponding finite-time Lyapunov exponents: (a) bifurcation diagram of the state variable v; (b) Lyapunov exponents with respect to the control parameter ω.

The consistent correspondence between bifurcation structures and Lyapunov exponents – particularly the alternation between negative exponents in periodic windows and positive LE1 in chaotic bands – quantitatively validates the frequency-induced transitions among quasi-static modulation, periodic bursting, chaos, and multi-periodic oscillations in the proposed second-order memcapacitor-based FHN neuron.

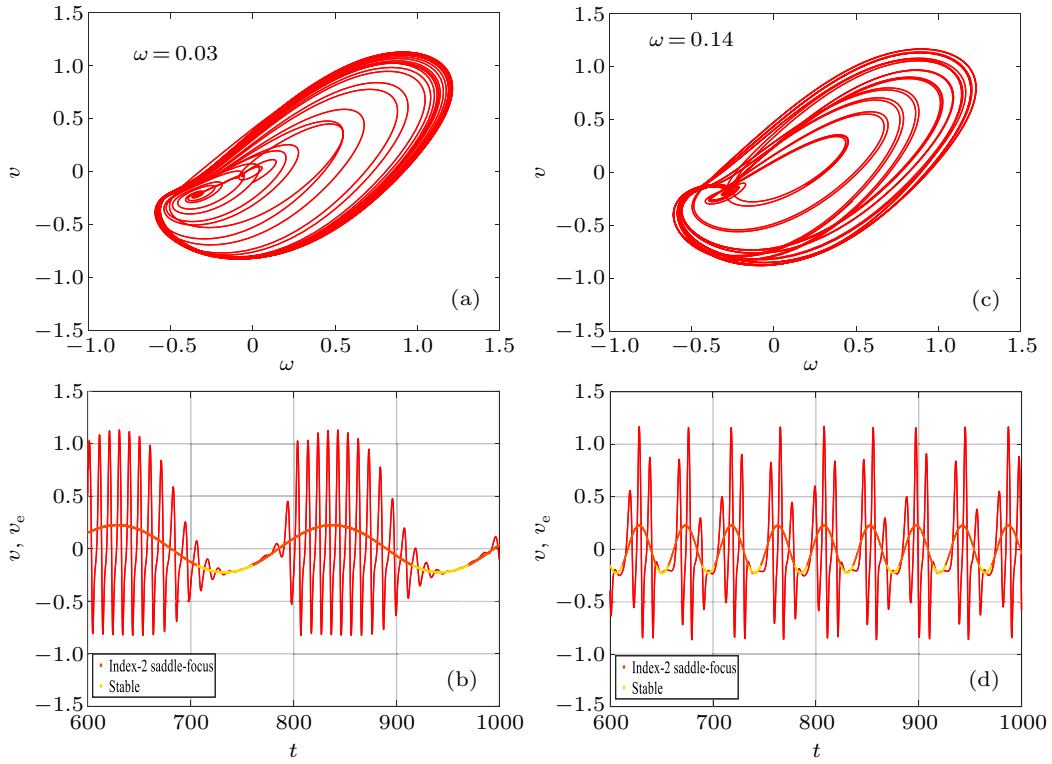


Fig. 5. Neural dynamics at low frequencies. The neuron exhibits strong tracking at $\omega = 0.03$ and partial modulation at $\omega = 0.14$.

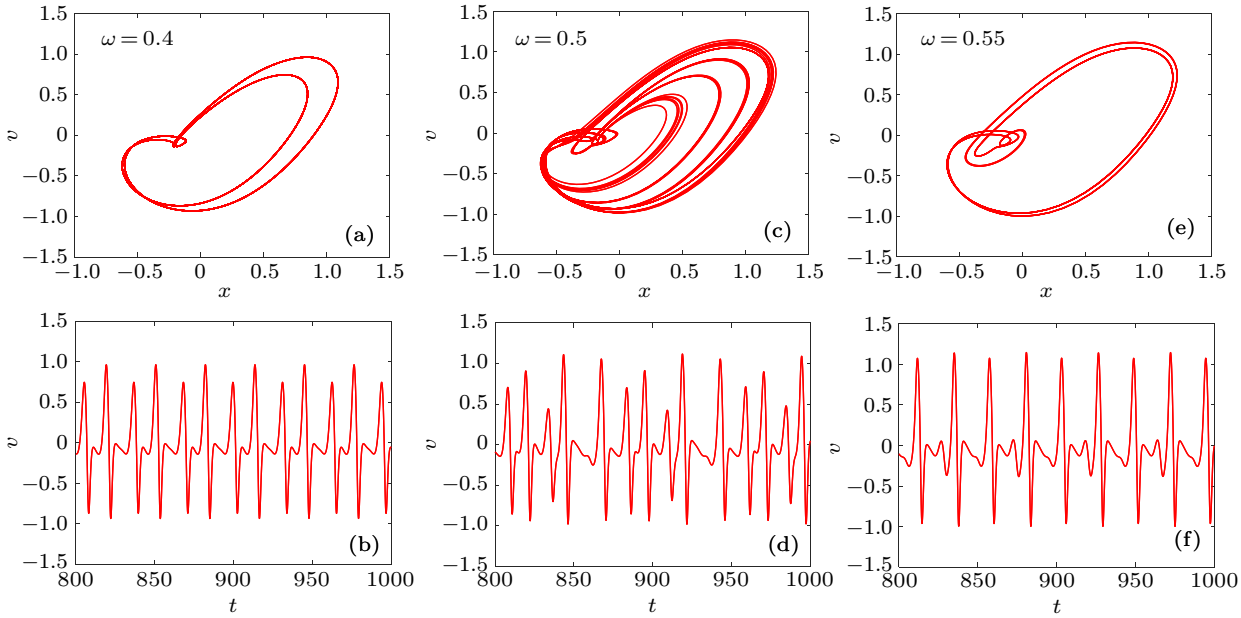


Fig. 6. Numerical simulation results of neuronal firing patterns under different angular frequencies ω. (a), (c), and (e) depict the phase portraits in the x–v plane for $\omega = 0.4$, 0.5, and 0.55, respectively. (b), (d), and (f) show the corresponding time-domain waveforms of v.

4.2. Excitation amplitude-dependent electrical activity

In this section, the effect of the excitation amplitude F on the firing dynamics of the second-order memcapacitor-based FHN neuron is examined. The excitation frequency is fixed at $\omega = 1.5$, and the initial conditions are held constant.

Figure 7(a) depicts the transition of the firing behavior as the excitation amplitude F varies in the range [0, 1.5], accompanied by the corresponding Lyapunov exponents shown in Fig. 7(b). Collectively, these plots reveal distinct transi-

tions induced by changes in amplitude among various firing regimes, characterized by fluctuations in the sign of the maximum Lyapunov exponent LE1. For $F \in [0, 0.38)$, the bifurcation diagram presents irregularly, widely scattered points while LE1 remains positive throughout this interval, confirming sustained chaotic dynamics. As illustrated in Figs. 8(a) and 8(b), the neuron displays complex chaotic oscillations. As F increases beyond 0.38, the chaotic firing is abruptly replaced by multiperiodic oscillations, indicative of a crisis-like transition associated with the sudden destruction of the chaotic attractor. As the amplitude increases to $F \in [0.38, 0.51)$, bifurcation branches converge into distinct bands and LE1 becomes negative, signaling a transition from chaos to periodic oscillations. At $F = 0.45$ (Figs. 8(c) and 8(d)), the phase portrait reveals regular closed orbits, and consistent periodic bursting is observed in the time series. With further increase in amplitude for $F \in [0.51, 0.93)$, λ_1 once again turns positive, marking a return to chaotic firing. This abrupt transition suggests the destabilization of multiperiodic attractors through a boundary crisis, leading to the recovery of chaotic firing behavior. At $F = 0.8$ (Figs. 8(e) and 8(f)), both the phase portrait and time series revert to irregular and complex patterns alongside a positive value for LE1. When considering amplitudes within $F \in [0.93, 1.5]$, the bifurcation diagram displays several smooth curves and the maxima of the Lyapunov exponent are negative, indicating that the neuron exhibits periodic oscillations. Figures 8(g)–8(j) present period-2 and single-periodic firing behaviors. This transition from chaos to periodicity occurs progressively within a narrow

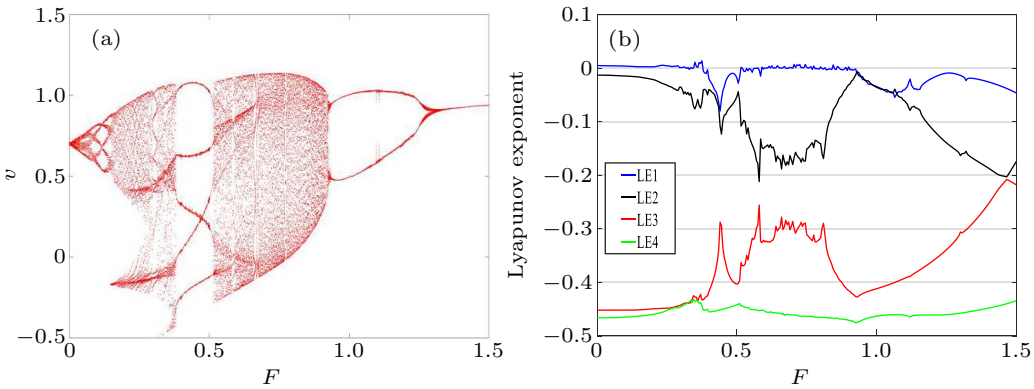


Fig. 7. Bifurcation diagram of state variable v and the corresponding finite-time Lyapunov exponent spectra: (a) the bifurcation diagram of the state variable v with respect to the control parameter F; (b) the diagram showing the four Lyapunov exponents.

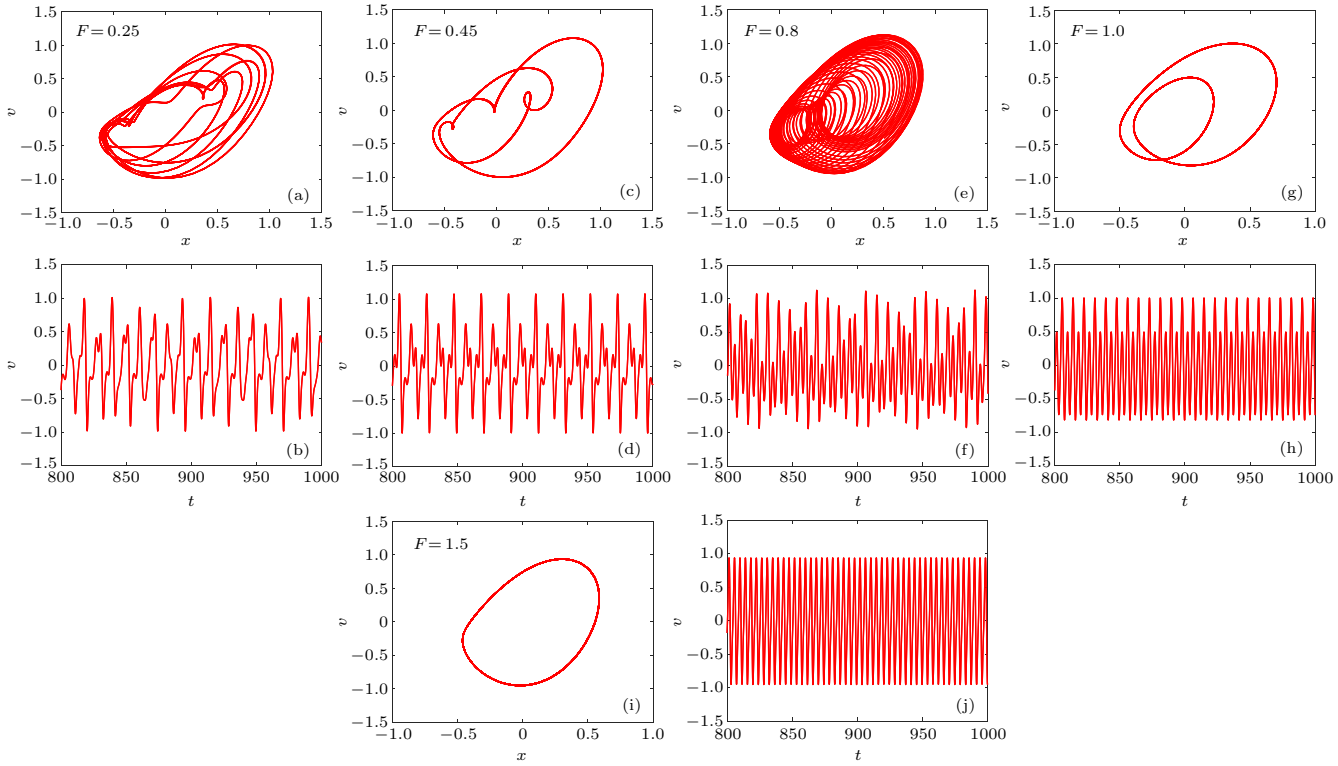


Fig. 8. Numerical simulation results of neuronal firing patterns under different F. (a), (c), (e), (g), and (i) depict the phase portraits in the x–v plane for $F = 0.25$, 0.45, 0.8, 1.0, and 1.5, respectively. (b), (d), (f), (h), and (j) show the corresponding time-domain waveforms of v.

parameter interval. During this interval, the chaotic attractor rapidly contracts and stabilizes via a reverse period-doubling process, ultimately resulting in period-2 and single-periodic firing behaviors.

These findings demonstrate that the excitation amplitude F serves as an effective control parameter capable of driving the neuron through successive dynamical transitions–from chaos to multiperiodicity, back to chaos–and finally to periodic regimes.

4.3. Firing dynamics under two-parameter modulation

This section examines the collective effects of the excitation amplitude F and frequency ω on the firing behavior of the second-order memcapacitor-based FHN neuron. A two-parameter dynamical map is constructed over the parameter domain $F \in [0, 1.5]$ and $\omega \in [1.5, 3]$, with the initial conditions set to $(0.1, 0.1, -0.1, 0.3)$, as shown in Fig. 9.

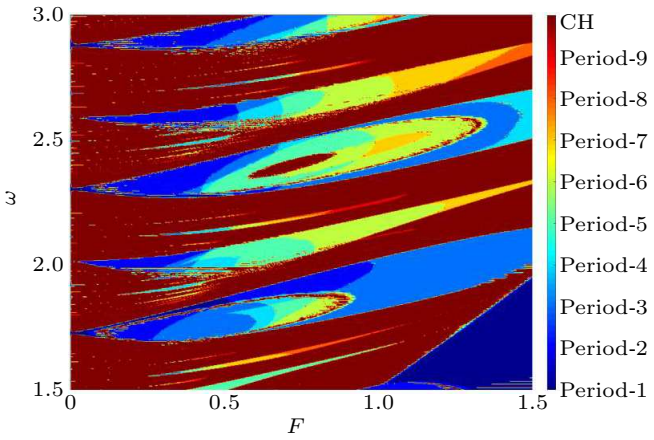


Fig. 9. Dynamical map with respect to the control parameters F and ω.

The resulting map classifies firing regimes based on periodicity and chaos: periodic states are color-coded according to their period (1–9), while regions where the firing period exceeds 9 are labeled "CH", indicating transitions to aperiodic and unpredictable dynamics. The diagram reveals rich, structured patterns of alternating periodic and chaotic zones, highlighting the sensitive and nonlinear coupling between F and ω in shaping neuronal activity.

This analysis illustrates that the neuron's firing mode can be systematically tuned by jointly varying amplitude and frequency, providing a comprehensive view of parameter-dependent transitions and underscoring the intricate interplay between external stimulation characteristics and the intrinsic dynamics endowed by the second-order memcapacitor.

4.4. Initial value-dependent electrical activity

This section investigates the phenomenon of multistability in the proposed second-order memcapacitor-based FHN neuron, in which distinct stable firing patterns coexist under identical system parameters but different initial conditions. Such multistability is fundamental to neuronal information processing and enriches the repertoire of dynamic behaviors. To analyze this effect, the control parameters are fixed at $F = 0.25$, $\omega = 0.9$, and $\lambda = -0.27$, with the initial condition $(x(0), y(0)) = (0, 0)$. Two bifurcation analyses are performed by varying the initial conditions of the memcapacitor's internal state variables $z(0)$ and $e(0)$, respectively.

Figure 10(a) illustrates the bifurcation diagram of the membrane voltage v as a function of the initial state $z(0)$, with $e(0) = 0$. The diagram reveals clear transitions between periodic and chaotic firing regimes as $z(0)$ varies, manifested as alternating bands of periodic branches and scattered chaotic points. Similarly, Fig. 10(b) presents the corresponding diagram when varying the initial slow variable $e(0)$ while keeping $z(0) = 0$. Despite differences in the distribution ranges of periodic and chaotic regions between the two diagrams, the geometric structure and width of the resulting attractors exhibit remarkable similarity in phase space. This similarity is further illustrated in Fig. 11, which displays coexisting attractors for selected initial conditions. Figure 11(a) displays the coexisting periodic (blue) and chaotic (red) attractors for two different $z(0)$ values, while Fig. 11(b) presents the coexisting periodic (blue) and chaotic (red) attractors for two different $e(0)$ values. Despite the distinct initial conditions, the periodic and chaotic attractors in Figs. 11(a) and 11(b) show closely matched geometries, underscoring the robustness of the attractor morphology with respect to variations in the memcapacitor's internal initial states.

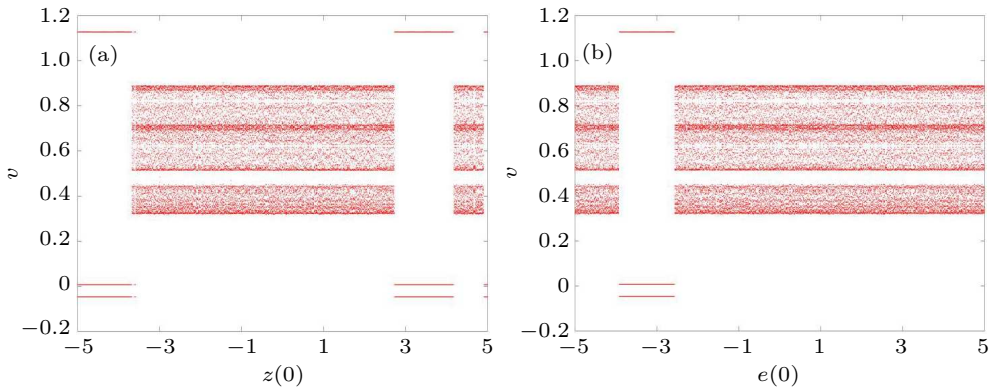


Fig. 10. Bifurcation diagrams showing the effect of initial conditions on neuronal firing patterns: (a) transitions between periodic and chaotic firing as $z(0)$ varies, (b) transitions as $e(0)$ varies.

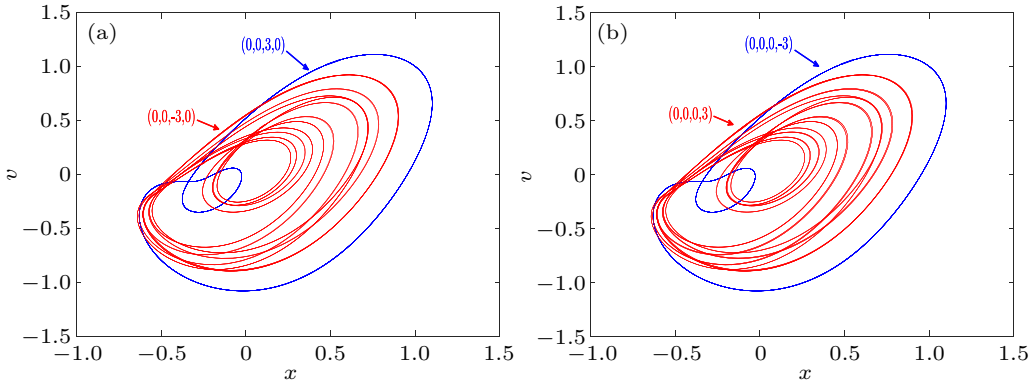


Fig. 11. Phase portraits showing the attractor dynamics for different initial conditions: (a) initial condition $(0,0,-3,0)$ (red) and $(0,0,3,0)$ (blue); (b) initial condition $(0,0,0,3)$ (red) and $(0,0,0,-3)$ (blue).

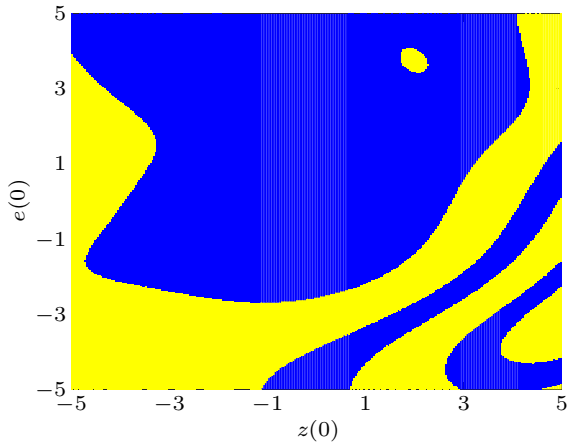


Fig. 12. Basins of attraction on the $z(0)$–$e(0)$ plane, showing chaotic behavior (blue) and periodic firing (yellow) based on initial conditions.

To characterize the basins of attraction, Fig. 12 maps the asymptotic behavior on the $z(0)$–$e(0)$ plane for $x(0) = 0$ and $y(0) = 0$. The plane is divided into two well-defined regions: a yellow zone corresponding to periodic firing and a blue zone corresponding to chaotic dynamics. The basin boundary exhibits a complex, intertwined structure, confirming that the neuron's long-term behavior depends sensitively on the initial conditions of the memcapacitor's internal variables.

These results demonstrate that the second-order memcapacitor not only introduces multiscale memory but also enables pronounced initial-condition-dependent multistability. By adjusting $z(0)$ and $e(0)$, the neuron can be selectively tuned into either regular periodic spiking or complex chaotic firing, offering a flexible mechanism for dynamically reconfiguring neuronal responses without changing circuit parameters. This feature holds significant potential for neuromorphic systems that require adaptive, history-sensitive information processing.

5. Other neuromorphic behaviors

The proposed FHN neuron demonstrates its capability to replicate a variety of classic firing behaviors observed in biological systems, reflecting the interplay between nonlinear dynamics and embedded multiscale memory. These behaviors emerge from specific combinations of external stimulus characteristics and internal parameter configurations. Figures 13(a)–13(h) illustrate eight representative firing patterns, where external stimuli are depicted in red and the corresponding intrinsic neuronal responses are shown in blue, highlighting the dynamic relationship between external driving and internal excitability. The successfully reproduced neuromorphic behaviors include phasic spiking (PS), tonic spiking (TS), mixed-mode oscillations (MO), subthreshold oscillations (SO), inhibition-induced spiking (IS), Class 2 excitability (C2), rebound spiking (RS), and bistability (BI). For each firing pattern, the neuron's initial state is consistently set to $(0,0,0,0.1)$. The specific forms of external stimulation and the corresponding internal parameter sets are systematically summarized in Table 1. The table provides explicit references to the respective subfigures, offering a clear mapping between stimulation paradigms, parameter choices, and the resulting firing patterns. This comprehensive reproduction of canonical

Table 1. External stimulus functions and corresponding internal parameters for each discharge mode, with references to the corresponding figures.

Firing pattern	External stimulus	a_1	b_1	a_2	b_2	α	β	λ	a	c	Fig.
PS	$I(t) = 0.5$ for $50 \le t \le 55$	0.8	0.5	0.5	0.5	1.0	0.6	−0.3	1.0	1.0	13(a)
TS	$I(t) = 0.01$ for $200 \le t \le 600$	0.8	0.5	0.5	0.5	1.0	0.5	−0.5	1.0	1.0	13(b)
MO	$I(t) = 0.01$ for $200 \le t \le 600$	0.8	0.5	2.6	0.02	1.0	0.5	−1.0	1.8	0.44	13(c)
SO	$I(t) = 0.01$ for $50 \le t \le 60$	0.8	0.1	0.5	0.1	1.0	0.5	−0.3	0.5	0.7	13(d)
IS	$I(t) = -0.1$ for $200 \le t \le 220$	0.8	0.5	0.5	0.5	1.0	0.5	−0.5	1	0.6	13(e)
C2	$I(t) =$ linear increase from 0 to 5×10^{-6} for $100 \le t \le 600$	0.8	0.5	0.6	0.4	0.8	0.3	−0.1	0.6	0.55	13(f)
RS	$I(t) = -0.1$ for $50 \le t \le 55$	0.8	0.5	0.5	0.5	1.0	−0.6	1.0	1.0	1.0	13(g)
BI	$I(t) = 0.01$ for $100 \le t \le 200$, $I(t) = -0.1$ for $400 \le t \le 600$	0.8	0.5	0.5	0.5	1.0	0.6	−0.4	1.0	0.6	13(h)

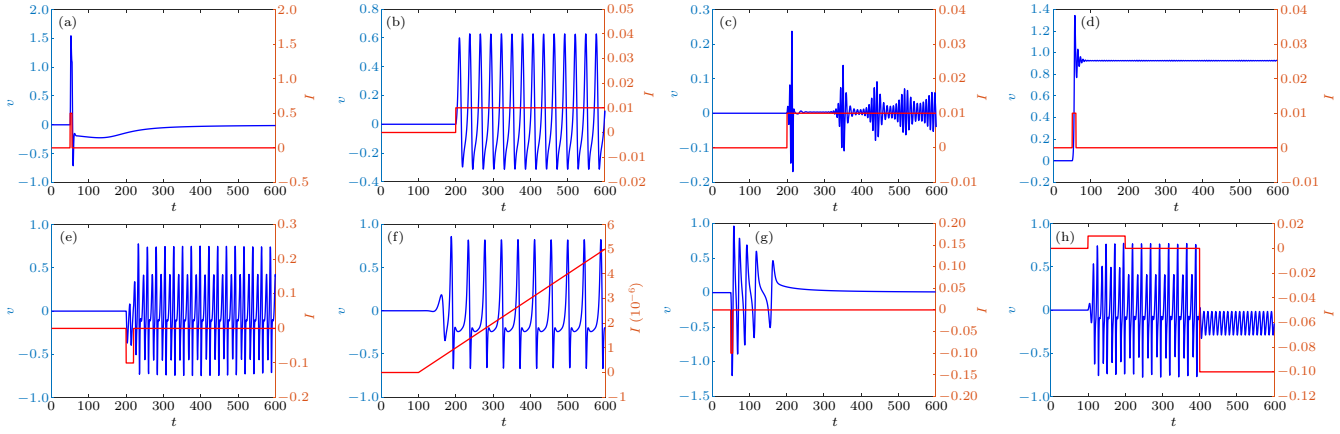


Fig. 13. Classic firing patterns of the second-order memcapacitor-based FHN neuron, with external stimuli marked in red and intrinsic firing behavior in blue. (a) Phasic spiking; (b) tonic spiking; (c) mixed-mode; (d) subthreshold oscillations; (e) inhibition-induced spiking; (f) class-2 excitability; (g) rebound spike; (h) bistability.

behaviors not only validates the biological plausibility of the model but also underscores its versatility for emulating diverse neural coding schemes in neuromorphic hardware implementations.

6. Circuit implementation

To validate the physical realizability of the proposed model, a modular analog circuit corresponding to the second-order memcapacitor-based FHN neuron is designed and simulated using off-the-shelf electronic components. The circuit parameters are fixed as: $a_1 = 0.8$, $b_1 = 0.5$, $a_2 = 0.5$, $b_2 = 0.5$, $\alpha = 1.0$, $\beta = 0.5$, $\lambda = -0.3$, $a = 1$, and $c = 0.6$, consistent with the numerical analyses conducted earlier. The corresponding neuron circuit is designed using conventional electronic components, following a modular design approach, as illustrated in Fig. 14. According to Kirchhoff's laws, the corresponding circuit equations can be written as

$$\begin{cases} V_v = g_1 V_y \left(-\dfrac{R_3}{R_5}(-1) - \dfrac{R_3}{R_4}(-V_z) - \dfrac{R_3}{R_6}\tanh(V_e) \right), \\ R_0 C_0 \dfrac{\mathrm{d}V_x}{\mathrm{d}t} = -\dfrac{R_0}{R_7}V_x - \dfrac{R_0}{R_8}(-V_v), \\ R_0 C_0 \dfrac{\mathrm{d}V_y}{\mathrm{d}t} = -\dfrac{R_0}{R_{11}}(-F\cos\omega t) - \dfrac{R_0}{R_{10}}(-V_v) \\ \qquad\qquad - \dfrac{R_0}{R_{12}}(V_x) - \dfrac{R_0}{R_9}(g_2 g_3 V_y^3), \\ R_0 C_0 \dfrac{\mathrm{d}V_z}{\mathrm{d}t} = -\dfrac{R_0}{R_{13}}(-V_y) - \dfrac{R_0}{R_{14}}V_z, \\ R_0 C_0 \dfrac{\mathrm{d}V_e}{\mathrm{d}t} = -\dfrac{R_0}{R_{15}}(-g_4 V_y^2) - \dfrac{R_0}{R_{16}}\tanh(V_e), \end{cases} \tag{9}$$

where the state variables V_x, V_y, V_z, and V_e correspond to the capacitor voltages in their respective integrator circuits, with a time constant of $R_0 C_0 = 1$ s ($R_0 = 1$ MΩ and $C_0 = 1$ μF). In addition, the gains of the four multipliers are $g_1 = g_2 = g_3 = g_4 = 1$. The values of the resistors are set as follows: $R_w = 10$ kΩ, $R_1 = 520$ Ω, $R_2 = 1$ kΩ, and $R_3 = 3$ kΩ.

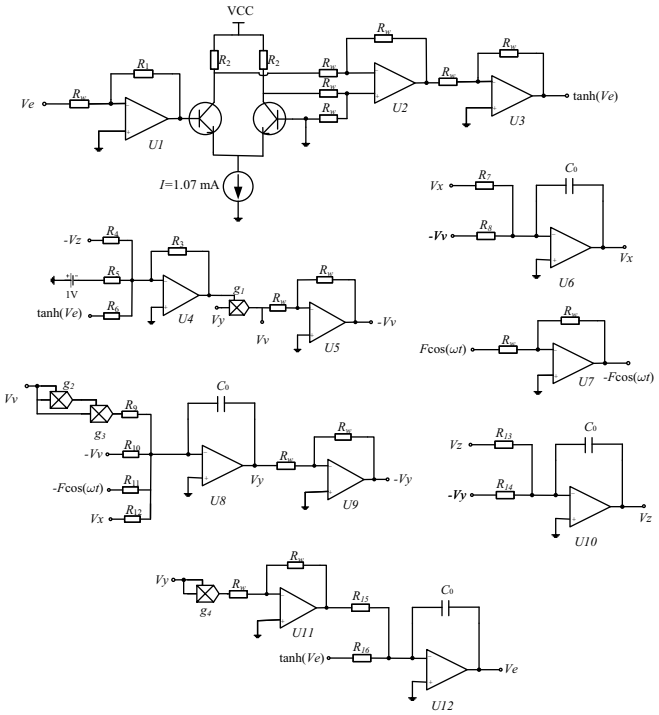


Fig. 14. Schematic diagram of the second-order memcapacitor-based FHN circuit.

By comparing Eq. (5) with Eq. (9), the circuit component values can be straightforwardly derived from the following relationships:

$$R_4 = \frac{R_3}{0.5}, \quad R_5 = R_3, \quad R_6 = \frac{R_3}{0.3}, \quad R_7 = \frac{R_0}{0.6}, \quad R_8 = R_0,$$
$$R_9 = 3g_2 g_3 R_0, \quad R_{10} = R_0, \quad R_{11} = R_0, \quad R_{12} = R_0,$$
$$R_{13} = \frac{R_0}{0.8}, \quad R_{14} = \frac{R_0}{0.5}, \quad R_{15} = \frac{R_0}{0.5}, \quad R_{16} = \frac{R_0}{0.5},$$

and the corresponding circuit component values are summarized in Table 2.

The initial conditions are configured via the initial voltages of the integrating capacitors: $V_{x_0} = V_{y_0} = 0.1$ V, $V_{z_0} = -0.1$ V, and $V_{e_0} = 0.3$ V, and four different conditions are examined. First, the amplitude of the constant external stimulus

is fixed at $F = 0.125$ with $\omega = 0.03$ and $\omega = 0.4$. Second, the frequency ω is fixed at 1.5 with $F = 0.25$ and $F = 0.45$.

Table 2. FHN neuron circuit parameter settings.

Parameters	Significations	Values
R_w	resistance	10 kΩ
R_0	resistance	1000 kΩ
R_1	resistance	520 Ω
R_2	resistance	1 kΩ
R_3	resistance	3 kΩ
R_4	resistance	6 kΩ
R_5	resistance	3 kΩ
R_6	resistance	10 kΩ
R_7	resistance	1666 kΩ
R_8	resistance	1000 kΩ
R_9	resistance	3000 kΩ
R_{10}	resistance	1000 kΩ
R_{11}	resistance	1000 kΩ
R_{12}	resistance	1000 kΩ
R_{13}	resistance	1250 kΩ
R_{14}	resistance	1000 kΩ
R_{15}	resistance	2000 kΩ
R_{16}	resistance	2000 kΩ
C_0	capacitance	1 μF

The circuit simulation results exhibit excellent agreement with the numerical predictions presented in Section 4. For example, under $F = 0.125$ and $\omega = 0.03$, the neuron exhibits bursting oscillations, with the corresponding phase portrait and time series shown in Figs. 15(a) and 15(b). When $F = 0.125$ and $\omega = 0.4$, the neuron displays period-2 firing, as illustrated in Figs. 15(c) and 15(d). For $\omega = 1.5$ and $F = 0.25$, chaotic firing is observed in Figs. 15(e) and 15(f). Under $\omega = 1.5$ and $F = 0.45$, multi-periodic firing patterns are clearly observed (Figs. 15(g)–15(h)). These correspondences confirm both the correctness of the circuit implementation and the consistency of the dynamical behaviors predicted by the model. In practical hardware, non-ideal factors such as resistor/capacitor tolerances and circuit noise may perturb the effective parameters of the emulator. As a result, the boundaries between periodic and chaotic regimes may shift, and the waveforms may exhibit small jitter. To evaluate the robustness against parameter uncertainties, the experimental parameters were selected as $\omega = 1.5$ and $F = 1$. Capacitance deviations of $\pm 2.5\%$ and $\pm 5\%$ were introduced, resulting in four tolerance scenarios. The corresponding results are presented in Fig. 16.

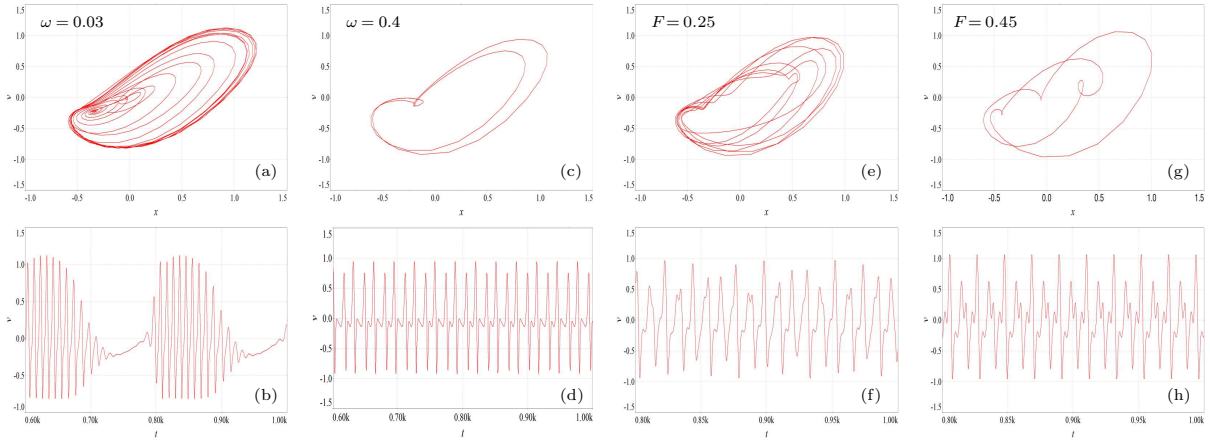


Fig. 15. Phase portraits and time series of the second-order memcapacitor-based FHN neuron circuit. The experimental results agree well with the simulation results in Section 4, confirming the correctness of the circuit implementation.

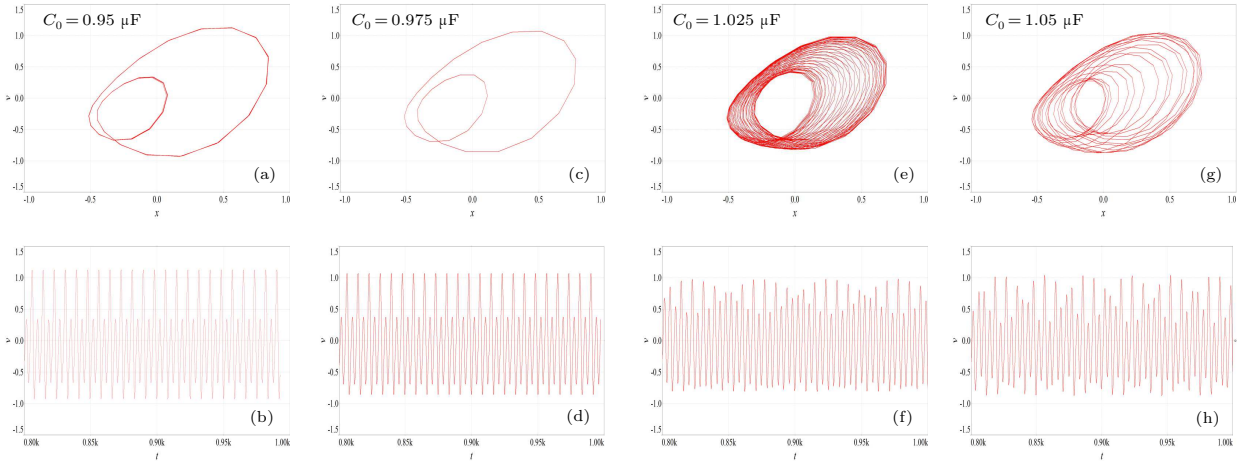


Fig. 16. Phase portraits under capacitance deviations of $\pm 2.5\%$ and $\pm 5\%$ at $\omega = 1.5$ and $F = 1$, where (a), (c), (e), and (g) correspond to different tolerance scenarios. The corresponding time series are shown in (b), (d), (f), and (h), respectively.

It can be observed that negative capacitance deviations mainly influence the oscillation amplitude without altering the firing mode, whereas positive deviations lead to a modification of the firing pattern and a shift of the chaos–period transition boundary. This indicates that the system exhibits asymmetric sensitivity to parameter perturbations while preserving its overall dynamical structure.

7. Conclusion

This study has successfully integrated a secondorder memcapacitor into the FHN neuron model, establishing a novel fourdimensional dynamical system capable of emulating multiscale memory mechanisms. By introducing fast and slow internal state variables, the memcapacitor enables simultaneous representation of shortterm adaptation and longterm plasticity within a single compact device, addressing a critical gap in existing neuromorphic implementations. Comprehensive numerical analyses, including bifurcation diagrams, Lyapunov exponents, and twoparameter dynamical maps, systematically revealed the influence of excitation frequency, amplitude, and initial conditions on the neuron's firing behavior. The system exhibits rich dynamical transitions among periodic, multiperiodic, and chaotic regimes, alongside pronounced multistability originating from the memcapacitor's internal states. Furthermore, the model successfully reproduces eight canonical neuromorphic firing patterns, demonstrating its biological plausibility and functional versatility. An analog circuit was designed and implemented using standard electronic components to physically realize the proposed neuron. Simulation results align closely with numerical predictions across multiple operational regimes, validating both the mathematical model and its hardware feasibility.

In summary, this work contributes a biologically grounded, yet hardware-efficient, neuron model enriched by dual-timescale memory. The second-order memcapacitor not only extends the dynamic repertoire of the FHN system but also provides a practical pathway toward building adaptive, low-power neuromorphic circuits. Future work will focus on extending the proposed neuron model to memcapacitor-based neural networks, enabling the investigation of network-level dynamics such as synchronization, multistability, and collective firing patterns. In particular, incorporating learning and adaptation mechanisms at the network level, such as activity-dependent coupling or synaptic plasticity, will allow the exploration of how memory-enhanced neurons support self-organized and adaptive neural computation.

Acknowledgments

This project is supported by the National Natural Science Foundation of China (Grant No. 62171401) and the Key Project of the Education Department of Hunan Province (Grant No. 25A0146).

References

[1] Apata C O, Tang Y R, Zhou Y F, Jiang L and Pei Q M 2024 *Chin. Phys. B* **33** 058704

[2] Kumar P and Erturk V S 2025 *Chin. Phys. B* **34** 018704

[3] Huang L L, Huang Q, Zang H Y, Lei T F, Fu H Y and Gao F 2025 *Phys. Scr.* **100** 065232

[4] Catterall W A, Raman I M, Robinson H P C, Sejnowski T J and Paulsen O 2012 *J. Neurosci.* **32** 14064

[5] Wang X, Jia K and Ge M 2025 *Chin. J. Phys.* **97** 1355

[6] Peng Y X, Li M L, Li Z J, Ma M L, Wang M J and He S B 2025 *Neural Netw.* **185** 107213

[7] Liu Z W, Mei J, Tang J S, *et al.* 2025 *Nat. Electron.* **8** 362

[8] Deng Q L, Wang C H and Yang G 2025 *Int. J. Bifurcation Chaos* **35** 2550053

[9] Yang F F, Ma J and Wu F Q 2024 *Chaos Solitons Fractals* **187** 115361

[10] Romero F J, Ohata A, Toral-Lopez A, Godoy A, Morales D P and Rodriguez N 2021 *Electronics* **10** 1225

[11] Di Ventra M, Pershin Y V and Chua L O 2009 *Proc. IEEE* **97** 1717

[12] Chen Y X, Cao Y H, Mou J, Sun B and Banerjee S 2024 *Int. J. Bifurcation Chaos* **34** 2450069

[13] Njitacke Z T, Doubla I S, Mabekou S and Kengne J 2020 *Chaos Solitons Fractals* **137** 109785

[14] Qiao S, Gao C H and An X L 2023 *Nonlinear Dyn.* **111** 10529

[15] Wang X J, Wang H, Gu H G, Jia Y B and Li Y Y 2025 *Commun. Nonlinear Sci. Numer. Simul.* **151** 109086

[16] Wu H G, Gu J X, Wang N, Chen M and Xu Q 2025 *Chaos Solitons Fractals* **192** 115969

[17] Han Z T, Al-Barakati A A, Jahanshahi H and Mou J 2024 *Nonlinear Dyn.* **112** 4863

[18] Wang M J and Gu L F 2024 *Chin. Phys. B* **33** 020504

[19] Ma M L, Lu Y P, Li Z J, Sun Y C and Wang C H 2023 *Fractal Fract.* **7** 82

[20] Wang X, Mou J, Cao Y H and Jahanshahi H 2025 *Int. J. Bifurcation Chaos* **35** 2530010

[21] Ge M Y, Jia K, Wang X, Liu Y J and Jiang Y Q 2025 *Nonlinear Dyn.* **113** 26671

[22] Yin Z Y, Tian H, Chen G H and Chua L O 2015 *IEEE Trans. Circuits Syst. II* **62** 402

[23] Wang X Y, Yu J, Jin C X, Iu H H C and Yu S M 2019 *Nonlinear Dyn.* **96** 161

[24] Kim S, Du C, Sheridan P, Ma W, Choi S and Lu W D 2015 *Nano Lett.* **15** 2203

[25] Mikheev V, Chouprik A, Lebedinskii Y, *et al.* 2019 *ACS Appl. Mater. Interfaces* **11** 32108

[26] Khanas A, Hebert C, Becerra L, Portier X and Jedrecy N 2022 *Adv. Electron. Mater.* **8** 2200421

[27] Gao F, Dong Y J, Lei T F, Huang L L and Fu H Y 2025 *Phys. Scr.* **100** 085246

[28] Gao Z X, Zhao L L, Ge M J, Zhai D S, Wang Y Q, Guo J J and Xiao X 2025 *Jpn. J. Appl. Phys.* **64** 020905